Nanoscale Advances

ROYAL SOCIETY OF CHEMISTRY

PAPER

View Article Online
View Journal | View Issue

Check for updates

Cite this: *Nanoscale Adv.*, 2024, **6**, 5889

NIR-triggered photooxygenation of α-terpinene with upconversion nanohybrids†

Laura Francés-Soriano, ‡ Delia Bellezza,‡ Juan Ferrera-González, María González-Béjar * and Julia Pérez-Prieto *

Received 26th June 2024
Accepted 11th September 2024

DOI: 10.1039/d4na00528g

rsc.li/nanoscale-advances

Upconversion nanohybrids (UCNHs) consisting of rose bengal (RB) and upconversion nanoparticles (UCNPs) are able to promote terpinene oxidation upon near-infrared irradiation. The photophysical events occurring upon NIR-irradiation of the UCNH correlate well with the synthetic protocol used to prepare the UCNHs (RB loading and aggregation). These results highlight the importance of the optimization of UCNH composition for the photocatalysis outcome.

Open Access Article. Published on 11 September 2024. Downloaded on 12/28/2024 3:40:09 PM.
This article is licensed under a Creative Commons Attribution-NonCommercial 3.0 Unported Licence.

Introduction

Photocatalysts have been used in organic synthesis because of their inherent potential to implement organic transformations, which may be otherwise non-feasible under mild and green conditions.[1] In this context, photocatalyzed oxidations involving molecular oxygen as a reactant are of great interest since they can form carbon–oxygen and heteroatom–oxygen bonds.[2,3]

Near-Infrared (NIR) radiation accounts for ≈50% of the solar spectrum and offers fewer health risks and side reactions, as well as a deeper penetration than ultraviolet (UV) and visible (VIS) light through various reaction media.[4] NIR-triggered photocatalysis has emerged as a greener alternative in organic synthesis over UV-VIS photocatalysis.[5]

Positive photocatalysis to accomplish organic transformations triggered by NIR light can be direct and indirect, involving single and dual photoactive catalysts, respectively.[6] The direct one serves from molecular photocatalysts (PCs, *e.g.*, cyanines,[5,7] squaraines,[8] and so on) to absorb NIR-light. The indirect one serves from an upconverting system to absorb NIR-light, *e.g.*, upconversion nanoparticles (UCNPs) in which lower-energy photons are transformed into higher-energy photons. The upconverting system is combined with PCs (able to absorb the upconverted light). This combination is usually known as upconversion nanohybrid (UCNH). The major advantage of this strategy is that known PCs can be used to synthesize UCNHs.[4,6] NIR-excitation of UCNHs has proven useful for photoinduced reactions,[9] such as photopolymerization,[10] photoisomerization, and photocoupling.[11] For example, UCNHs containing $[Ru(bpy)_3]^{2+}$ as a PC have been used to accomplish the photoredox-catalysed aerobic oxidation of ethyl-2-bromo-2-phenylacetate.[4]

The attachment of a PC to a UCNP surface can confer upon the UCNH the ability to generate singlet oxygen ($^1O_2$) upon NIR excitation, since the PC can absorb the upconverted emission to generate singlet oxygen, a phenomenon previously demonstrated with numerous PCs.[12–23]

It would be expected that organic transformations carried out with the selected PC (absorption in the UV-VIS range) could easily be performed by using NIR light instead to activate the UCNHs containing the same PC.

In this context, we have recently prepared a colloidal UCNH made of a xanthenic dye, in particular rose bengal (RB), grafted to ytterbium and erbium co-doped upconversion nanoparticles (UC_{Er}) to study the fundamental mechanisms which govern the dye photophysics upon interaction with the UCNPs.[24] Moreover, among the previously reported UCNHs made up of UCNPs and RB,[15,24–29] the generation of singlet oxygen ($^1O_2$) has been identified[15,28] upon NIR-irradiation of UCNHs with a similar composition.

RB has been extensively used for visible light–driven reactions because the RB triplet excited state (^{3}RB) transfers energy to ground state oxygen ($^3O_2$) to give singlet oxygen $^1O_2$.[30] The photooxygenation of α-terpinene has been extensively evaluated with heterogeneous systems containing RB as the PC, thereby facilitating the separation process and avoiding RB photodegradation.[31–34] We envisaged that the synthesized UC@RBn NHs could serve as heterogeneous NIR-photocatalysts.

Up to now, the influence of photoactive lanthanides doping the UCNP and PC loading on the photocatalytic activity of UCNHs remains unexplored. The preparation of UCNHs is not

Instituto de Ciencia Molecular (ICMol), Departamento de Química Orgánica, Universitat de València, Calle Catedrático José Beltrán 2, Paterna, Valencia 46980, Spain. E-mail: maria.gonzalez@uv.es; julia.perez@uv.es

† Electronic supplementary information (ESI) available: Materials, methods, TEM images, TGA, emission spectra, kinetic profiles, emission decay fittings, phosphorescence spectra, transient absorption spectra, laser-induced emission spectra, ABDA photoconsumption spectra, and ^{1}H-NMR spectra. See DOI: https://doi.org/10.1039/d4na00528g

‡ These authors contributed equally.

© 2024 The Author(s). Published by the Royal Society of Chemistry

Open Access Article. Published on 11 September 2024. Downloaded on 12/28/2024 3:40:09 PM.
This article is licensed under a Creative Commons Attribution-NonCommercial 3.0 Unported Licence.

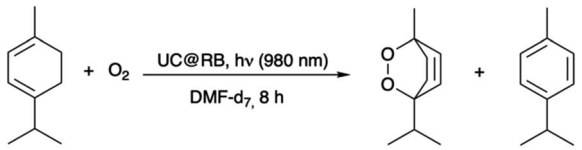

Scheme 1 NIR-triggered photooxidation of α-terpinene catalysed by UC@RB to give ascaridole and *p*-cymene (by-product).

a trivial task and we presumed that the photocatalytic performance of each UCNH would be strongly dependent on its photophysical properties. We have prepared and thoroughly characterized several UC@RB NHs with varying RB amounts.

To evaluate their capability to generate singlet oxygen, the photooxygenation of α-terpinene to produce ascaridole was tested as a benchmark reaction (Scheme 1). This work presents a comparative analysis between the photophysical properties of several UC_{Er}@RB NHs and their photocatalytic outcome upon NIR-irradiation.

Results and discussion

Functionalization of UCNPs with RB and characterization

Oleate-capped β-$NaYF_4$:Yb^{3+} (20%), Er^{3+} (2%) UCNPs (UC@OA) were synthesized by using a well-known thermal decomposition method with some modifications, as detailed in the ESI.†[35] The transmission electron microscopy (TEM) image (Fig. S1†) showed homogeneous hexagonal prisms of UC@OA with a size of 21.0 ± 0.8 × 18.9 ± 0.7 nm.

Functionalization with RB was achieved by following a two-step synthetic procedure (see the ESI†).[24] First, the oleate was removed from the UC@OA surface by treatment with $NOBF_4$. Then, oleate-free UCNPs were mixed with different RB concentrations ranging from 4.2×10^{-2} to 4.2×10^{-7} M (see the Experimental section for further details) in DMF for 24 hours, leading to the formation of different nanohybrids UC@RB1, UC@RB2, UC@RB3, UC@RB4, UC@RB5, and UC@RB6. The purification of the synthesized UC@RBn ($n = 1$–6) nanohybrids was based on cycles combining washing with DMF and centrifugation until the supernatant was colourless. Consequently, the number of cycles differed. Therefore, the lower the RB concentration, the lower the volume of DMF needed for washing UC@RBn. The dispersions of different UC@RBn nanohybrids in DMF resulted in pink dispersions with varying shades.

Among them, the most colourful was UC@RB2 (Fig. 1) thus indicating that the degree of RB aggregation in the starting stock solutions, aimed at preparing UC@RBn NHs, leads to less attachment.

To quantify the amount of RB attached to the UCNP surface, the RB concentration was estimated from each UC@RBn NH absorption spectrum after scattering subtraction. Considering the number of UCNPs in 1 mg of UCNH[36] and the RB moles derived from the absorbance, we initially estimated 34 ± 2, 104 ± 6, 98 ± 6, 6 ± 1, 1 ± 1, and 0.0 ± 0.1 RB molecules per UCNP for UC@RB1, UC@RB2, UC@RB3, UC@RB4, UC@RB5, and UC@RB6, respectively. It is noteworthy that these values are similar to those calculated in our previous work (20 RB/UCNP).[24]

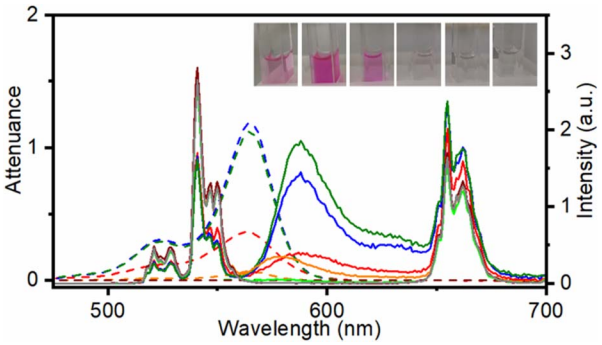

Fig. 1 Attenuance (dashed line) and emission spectra ($\lambda_{exc} = 980$ nm) normalized at 843 nm of dispersions in DMF at 1 mg mL^{-1} of UC@RB1 (red), UC@RB2 (blue), UC@RB3 (green), UC@RB4 (orange), UC@RB5 (light green), UC@RB6 (brown), and UC@OA (grey). Inset: photographs of the different dispersions in DMF of the UC@RB nanohybrids. From right to left: UC@RB1, UC@RB2, UC@RB3, UC@RB4, UC@RB5, and UC@RB6.

Photophysical characterization of UC@RBn nanohybrids

To evaluate the influence of the RB concentration on the photophysical properties of the UC@RBn NHs, their absorption and emission spectra were recorded in dimethylformamide (DMF). The absorption spectra of the UC@RBn dispersions should exhibit a consistent trend of increasing absorption as the amount of RB on the NH increases. Notably, the absorption of UC@RB2 and UC@RB3, containing ~104 RB/UCNP or with 98 RB/UCNP exceeded that of UC@RB1, with 34 RB/UCNP (Fig. 1). This is consistent with previous results, where RB aggregates were observed when preparing UCNHs with more than 100 RB molecules per UCNP. In these UCNHs, RB was covalently linked to a ligand coating the UCNPs.[15] Absorption spectra revealed a band centered at 560 nm with a shoulder at shorter wavelengths (λ_{max}: 523 nm), which enhances with an increasing RB concentration due to the presence of RB dimers or higher order aggregates. We previously hypothesized that the aggregation of RB molecules occurred on the surface of the NPs due to concentration-induced aggregation or by interaction with the positively charged surface of UCNPs.[24] The fact that UC@RB1 presents the highest A_{560}/A_{522} ratio can be attributed to a pre-aggregation of RB molecules in the stock solution. This pre-aggregation could lead to the direct attachment of RB dimers/aggregates to the UCNP surface. Moreover, the thermogravimetric analysis revealed a total mass loss of 26.1% that corresponds to 2286 ± 26 RB molecules attached to the surface of the UCNPs (Fig. S2†). Consequently, the number of RB molecules in UC@RB1 would be higher than 34, estimated from the absorption spectrum.

Fluorescence quantum yield (Φ_F) of RB in UC@RB dispersions supports this hypothesis (see Fig. 2).

All the UC@RBn NHs exhibited lower Φ_F as compared to free RB, with UC@RB1 showing a particularly notable decrease of approximately 30% despite having the largest RB loading.

© 2024 The Author(s). Published by the Royal Society of Chemistry

Open Access Article. Published on 11 September 2024. Downloaded on 12/28/2024 3:40:09 PM.
This article is licensed under a Creative Commons Attribution-NonCommercial 3.0 Unported Licence.

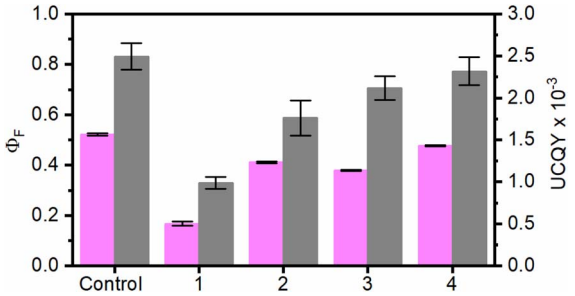

Fig. 2 Fluorescence quantum yield of RB (Φ_F; pink columns, λ_{exc} = 560 nm) and upconversion quantum yield (UCQY, grey columns, λ_{exc} = 980 nm) of UC@RBn NHs (n = 1–4). Control experiments correspond to RB for $\Phi_{F,RB}$ and UC@OA for UCQY.

As previously reported, the reduced emission can be attributed to the self-deactivation effect due to π–π interactions in the aggregates of RB present in UC@RB1 NHs.[24]

The emission spectrum of the RB singlet excited state (^{1}RB) in UC@RB2 is centered at 576 nm as reported for RB (Fig. S3†).

The lifetime of the ^{1}RB was estimated to be between 2 and 2.3 ns in all the NHs and free RB. Neither ^{1}RB emission nor the lifetime was sensitive to oxygen (see Fig. S3, 4 and Table S1†).

Under excitation at 980 nm, Yb^{3+} acted as a sensitizer, absorbing the incident light and subsequently transferring the energy to Er^{3+} cations. Accordingly, UC emission spectra of UC@RBn NHs displayed the characteristic emission bands of Er^{3+} ions in the UV, visible and NIR spectra (Fig. 1). The deactivation of Er^{3+} through emissive transitions resulted in six main bands: a very weak UV emission band centred at ∼410 nm was observed due to the $^2H_{9/2} \rightarrow {}^4I_{15/2}$ transition. Following this, two green bands were detected at ∼525 nm ($^2H_{11/2} \rightarrow {}^4I_{15/2}$) and ∼540 nm ($^4S_{3/2} \rightarrow {}^4I_{15/2}$), with the latter being the most intense in the original UC@OA. Additionally, a red emission band was observed at around 660 nm, corresponding to the transition $^4F_{9/2} \rightarrow {}^4I_{15/2}$. Finally, the $^4S_{3/2} \rightarrow {}^4I_{13/2}$ transition led to a broad emission band centred at *ca.* 842 nm (not shown).

Noteworthy quenching of the UC green emission by 36%, 42%, and 44% was observed for UC@RB1, UC@RB2, and UC@RB3, respectively (see Fig. S5†). The spectral overlap between the RB absorption and Er^{3+} green emission would explain the decrease of the UC emission in the NHs with a higher RB loading.

Interestingly, alongside the deactivation of UC emission, a new emission centered at 588 nm emerged, which would correspond to the sensitized RB emission. Accordingly, resonant energy transfer (RET) from the Er^{3+} of the UCNPs to RB resulted in a long-lived RB emission (∼50 μs; Table S2†); UC@RB3 exhibited the most intense emission followed by UC@RB2 and UC@RB1. These results were in accordance with the idea that higher RB concentrations during the synthesis led to the loading of non-fluorescent RB dimers/aggregates, consequently diminishing the fluorescence of RB on the UCNPs in the NH.

Time-resolved spectroscopy (λ_{exc} = 980 nm) was used to register the UC@RBs decays for all the emission bands (Fig. S6 and S7 and Table S2†). Non-significant differences were observed in lifetimes obtained in air or under N_2. The emission lifetime at 540 nm was strongly shortened by the presence of RB in UC@RB1, UC@RB2, and UC@RB3, while in UC@RB4 the lifetime of the green emission remained practically unchanged, likely due to the low quantity of RB on the surface.

Notably, the amount of RB in UC@RB4, UC@RB5, and UC@RB6 was not enough to induce significant quenching of the UC green emission in comparison to the initial UC@OA. Nevertheless, while UC@RB5 and UC@RB6 exhibited no detectable RB emission, UC@RB4 demonstrated a notable emission band. Despite the low UC quenching efficiency (less than 1%), the RB emission peak was comparable to that of the UC@RB1 NH, evidencing an efficient energy transfer from UCNPs to RB. Furthermore, the peak maximum shifted to 577 nm, precisely matching that of free RB. This indicates that in UC@RB4, RB molecules are likely in a similar environment as they would be free in solution, allowing them to emit light at their characteristic wavelength.

In our prior investigation, we noted a red-shifting of the RB emission on UC@RB in 5 mg mL^{-1} dispersions in DMF due to concentration-induced aggregation.[24] This effect was suppressed by using more dilute dispersions (1 mg mL^{-1}). However, even when recording the UC emission spectra at this concentration, the increased RB loading amount could influence the aggregation degree of the UC@RB NHs within the dispersion, subsequently affecting the RB emissive properties.

Concerning the UCQY, a dependence on the RB concentration at the UCNP surface was observed with UC@RB1, the most affected NH with a decrease of more than 50% (Fig. 2 and S8†). This is consistent with an efficient deactivation of the UC luminescence in the presence of RB, due to RET processes from the UCNPs to RB upon NIR excitation.

Nanosecond-laser flash photolysis was used to record the transient absorption spectra of RB (Fig. 3) in the UCNHs and RB in DMF (absorbance was 0.24 at 560 nm). As we previously reported, RB triplet excited state (^{3}RB) absorption spectra recorded for the UC@RB NHs exhibited three absorption bands at *ca.*

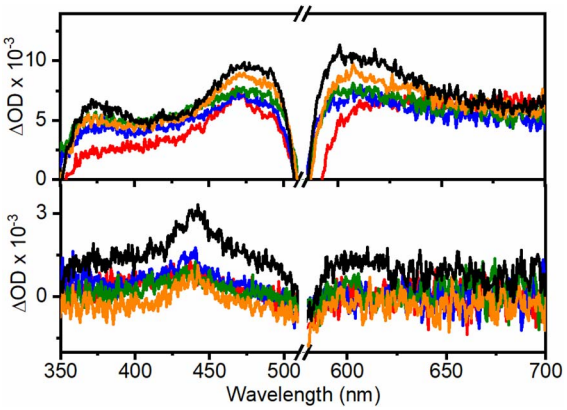

Fig. 3 Transient absorption spectra recorded at 20 ns (top) and 550 μs (bottom) after the laser pulse under N_2 (λ_{exc} = 560 nm, A = 0.24 at 560 nm) for UC@RB1 (red), UC@RB2 (blue), UC@RB3 (green), UC@RB4 (orange), and RB (black line) in DMF.

Open Access Article. Published on 11 September 2024. Downloaded on 12/28/2024 3:40:09 PM. This article is licensed under a Creative Commons Attribution-NonCommercial 3.0 Unported Licence.

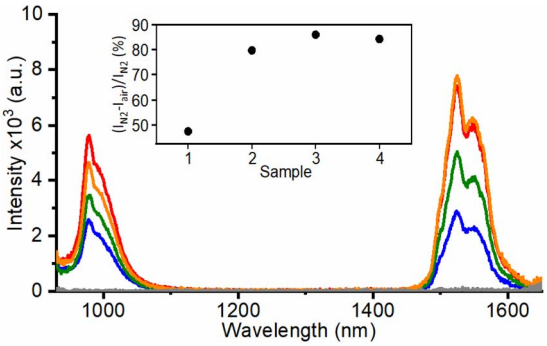

Fig. 4 NIR emission spectra (λ_{exc} = 560 nm) of UC@RBn in DMF (5 mg mL^{-1}) under N_2 for UC@RB1 (red), UC@RB2 (blue), UC@RB3 (green), and UC@RB4 (orange). Inset: ^{3}RB contribution in % for the different nanohybrids.

380, 470 and 610 nm.[24] The lower the number of RB molecules in the NH, the higher the absorbance of ^{3}RB in the spectra, which reveals better intersystem crossing (triplet formation). The generated ^{3}RB subsequently evolved into a RB radical anion ($RB^{\bullet-}$), which absorbs at *ca.* 440 nm (black trace in Fig. 3). However, when exciting RB in UC@RB, radical anion formation was clearly prevented for UC@RB2, UC@RB3 and UC@RB4, where ^{3}RB was almost exclusively generated, as compared to RB in solution and UC@RB1. As expected, O_2 quenched the ^{3}RB (Fig. S9†) in the UCNH revealing a fast process, close to a diffusion-controlled mechanism ($^3\tau_{RB}(O_2)$ shorter than 1 μs) (Table S3†).

As previously reported, room temperature phosphorescence of ^{3}RB (670–1300 nm; maximum at *ca.* 750 nm) was also observed with a lifetime >150 μs and, as expected, was quenched by oxygen (Fig. S10, S11 and Table S4†).

Moreover, laser induced emission measurements revealed ^{3}RB phosphorescence together with thermally activated delayed fluorescence under N_2 (Fig. S12†).

Remarkably, when RB in the UCNH was selectively excited at 560 nm, an antenna effect from RB to the photoactive lanthanide ions in UC@RB was also observed. Fig. 4 shows two intense bands centered at 975 and 1550 nm attributed to the $Yb^{3+}\cdot{}^2F_{5/2} \rightarrow {}^2F_{7/2}$ transition (the $Er^{3+}\cdot{}^4I_{11/2} \rightarrow {}^4I_{15/2}$ transition could play a minor role due to lower doping) and the $Er^{3+}\cdot{}^4I_{13/2} \rightarrow {}^4I_{15/2}$ transition, respectively. The emission intensities of these NIR bands at 975 nm (Yb^{3+} emission and ^{3}RB phosphorescence) and at 1550 nm (Er^{3+} emission) were quenched by O_2. Therefore, the emission bands registered in air were exclusively attributed to an energy transfer process from ^{1}RB, since ^{3}RB was efficiently deactivated in air (Fig. S13–S15 and Tables S5–S6†). Accordingly, the emission bands under an inert atmosphere are due to the energy transfer from ^{1}RB (46%) and ^{3}RB (54%) to the photoactive lanthanides.

Evaluation of 9,10-anthracenediyl-bis(methylene)dimalonic acid (ABDA) photoconsumption upon NIR-excitation of UC@RB nanohybrids

As stated above, upon NIR-irradiation of the UCNHs made up of UCNPs and RB, $^1O_2$ production was detected (either by using 1,3-diphenylisobenzofuran (DPBF), as an optical probe[28] or by direct detection of $^1O_2$ phosphorescence at 1270 nm).[15] Moreover, the optimal number of RB units for individual UCNPs has been determined to be ~100.[28] Even so, none of these UCNHs was used for synthetic purposes.

Here, we initially tested the NIR-driven $^1O_2$ generation of the UC@RB nanohybrids by using an anthracene-derivative, specifically 9,10-anthracenediyl-bis(methylene)dimalonic acid (ABDA), as a chemical $^1O_2$-trapping agent, since $^1O_2$ phosphorescence could not be detected spectroscopically under our experimental conditions.

The lifetime of singlet oxygen generation is solvent dependent.[37] Therefore, the efficiency of its generation can vary for each UCNH according to the solvent and was estimated for three solvents capable of affording colloidal dispersibility of the UC@RB nanohybrids while dissolving ABDA in dimethylformamide (DMF), acetonitrile (ACN), and ethanol (EtOH).

Next, the decrease in ABDA fluorescence due to the formation of its nonfluorescent endoperoxide was followed.[12] For this purpose, oxygen-saturated dispersions containing a mixture of UC@RB2 (with 100 RB/UCNP) and ABDA were irradiated with a 980 nm continuous wavelength laser diode to select the best solvent for the oxidation reaction. ABDA emission was recorded at different time intervals (Fig. 5). As shown in Fig. 5b and S16,† ABDA photoconsumption was observed in all solvents, indicating anthracene disappearance upon NIR-irradiation. The kinetic rates (k) of the process (monitored at 410 nm) are displayed in Table S7.† EtOH exhibited faster kinetics with a k value of 0.04, followed by ACN with a value of 0.024. However, ABDA photoconsumption did not progress after 2 hours of irradiation. Consequently, UC@RB2 dispersed in DMF was considered the most effective for ABDA photoconsumption, probably due to the superior dispersibility and stability of UC@RB in DMF.

Evaluation of photocatalytic activity of UC@RB nanohybrids

The photooxygenation of α-terpinene involves the addition of $^1O_2$ to the α-terpinene double bond, *i.e.*, a [4 + 2] cycloaddition,

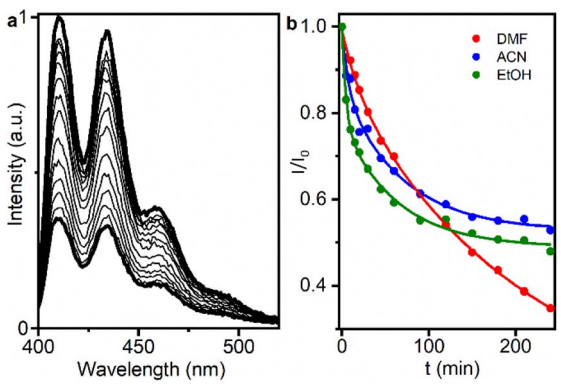

Fig. 5 (a) Decrease in ABDA emission intensity generated upon NIR excitation of UC@RB2 in DMF (at different time intervals). (b) Decrease in the ABDA emission intensity recorded at 410 nm upon different NIR exposure times (up to 240 min) for UC@RB2 dispersions (1 mg mL^{-1}) in DMF (red), ACN (blue), and EtOH (green).

© 2024 The Author(s). Published by the Royal Society of Chemistry

Open Access Article. Published on 11 September 2024. Downloaded on 12/28/2024 3:40:09 PM. This article is licensed under a Creative Commons Attribution-NonCommercial 3.0 Unported Licence.

Table 1 Conversion (%) of α-terpinene photocatalyzed by UC@RBn upon excitation at 980 nm for 8 h

N	PC	[UC@RB] (mg mL^{-1})	Ascaridole (%)	*p*-Cymene (%)
1	UC@RB1	1	12.4	4.1
2	UC@RB2	1	17.0	5.3
3	UC@RB3	1	16.5	4.7
4	UC@RB4	1	8.3	4.1
5	UC@BF_4	5	4.1	5.2
6	None	—	4.1	6.2
7	UC@RB3[a]	1	2.7	12.4
8	UC@RB2[b]	1	20.8	4.0
9	UC@RB3[c]	1	12.4	7.2
10	UC@RB2	5	41.3	3.1
11	UC@RB3	10	53.8	6.2
12	UC@RB2[d]	5	12.4	2.6
13	UC-RB	20	25.7	17.6
14	UC-RB[e]	20	19.2	17.1

[a] N_2. [b] 24 h. [c] CD_3CN. [d] Reaction performed with UC@RB recovered from entry 10. [e] Reaction performed with UC-RB recovered from entry 13.

resulting in the formation of ascaridole (Scheme 1) and autooxidation or dehydrogenation to *p*-cymene as a competitive reaction.[31–33] The capability of UC@RBn NHs to photocatalyze this reaction and generate ascaridole upon NIR excitation was assessed in deuterated DMF (DMF-d_7). For this purpose, an oxygen-saturated mixture of α-terpinene and the corresponding UC@RBn in DMF-d_7 was irradiated with a 980 nm continuous wavelength laser diode for 8 h. The conditions and conversion efficiencies toward ascaridole and *p*-cymene are detailed in Table 1.

The photocatalyst activity of UC@RBn upon NIR irradiation was evidenced by the formation of ascaridole in all cases. At a concentration of 1 mg mL^{-1} of the UC@RBn photocatalyst, the reaction yield for ascaridole formation was calculated to be 12.4%, 17%, 16.5%, and 8.3% for UC@RB1, UC@RB2, UC@RB3, and UC@RB4, respectively (entries 1–4 in Table 1). These yields were calculated by using ^{1}H-NMR spectroscopy after centrifugation to remove the NHs. UC@RB2 and UC@RB3 showed the best photocatalytic performance, which correlates well with their optical properties and corresponds to an RB/UCNP ratio of 100 (entries 2–3 in Table 1).

Control experiments with UCNPs without RB, in the absence of PC or oxygen (entries 5, 6 and 7, respectively), were carried out, thereby confirming that photooxidation was only possible in the presence of the UC@RBn NHs and O_2. Although α-terpinene and reaction products are colourless with absorption bands in the UV region (no absorption at 980 nm), small amounts of the by-product, *p*-cymene, were detected in all cases even in the absence of PCs (entry 5).

Longer reaction times (24 h) gave rise to a marginal increase in the formation of ascaridole, reaching 20.8%. This result can be attributed to the combined effect of photo- and thermal-degradation of products (entry 8).[38] Moreover, shorter reaction times of 1 and 4 h led to a lower ascaridole conversion, primarily due to the slow generation of singlet oxygen (Fig. S17†).

Alternatively, RB exhibits superior solubility and absorptivity in CD_3CN. However, the photocatalytic activity to get ascaridole was slightly lower (12.4%) (entry 9). Therefore, DMF-d_7 was selected as the solvent.

Then, experiments increasing the photocatalyst amount to 5 and 10 mg mL^{-1} were also conducted (entries 10 and 11). As a result, the yield of ascaridole reached 41.3% and 53.8%, respectively, after 8 hours of light exposure at 980 nm. Presumably, more $^1O_2$ would be generated by increasing the quantity of RB, thus resulting in a two-fold and three-fold enhancement in the selective production of ascaridole.

To assess the photocatalyst recyclability, the reaction mixture from entry 10 ([NH] = 5 mg mL^{-1}) was centrifuged (10 000*g*, 10 min), facilitating the precipitation of UC@RB2 NHs. Fresh α-terpinene and DMF-d_7 were added to the recovered UC@RB2 NH, and after redispersion, the mixture was irradiated at 980 nm for 8 h (Table 1, entry 12) yielding only 12.4% of ascaridole. The reduction of the photocatalytic activity can primarily be attributed to two factors: RB photobleaching and detachment of RB from the surface. In fact, partial photodegradation of RB was observed (*ca.* 20%). This points out that strategies to avoid PC leaching, such as covalent linking of the PC, should also be evaluated.

Consequently, we synthesized a previously reported NH in which RB is covalently linked to the UCNP surface, referred to as UC-RB,[15] and further investigated its photocatalytic performance. Briefly, the surface of UC@BF_4 was modified with 2-aminoethyl dihydrogen phosphate (AEP) and RB hexanoic ester (RB-HA) was linked *via* EDC/NHS chemistry.[15] To ensure comparability with the RB-grafted NH assays, equivalent RB concentrations were desired. Therefore, the UC-RB concentration (20 mg mL^{-1}) in the reaction mixture was adjusted to match the RB absorption observed in entry 10. Upon NIR irradiation, the total reaction yield was similar to that obtained with the non-covalent NH (*ca.* 43%). However, the reaction selectivity was significantly compromised, yielding 25.7% ascaridole and 17.6% *p*-cymene (Table 1, entry 13), which is almost half the ascaridole formation compared to the non-covalent NH. No RB leaching was observed after centrifugation of the sample (see Fig S18†). Notably, the recyclability experiment (Table 1, entry 14) evidenced a *ca.*25% reduction in the formation of ascaridole while keeping the yield towards *p*-cymene.

While UC-RB NHs exhibited superior resistance to PC leaching, the selectivity of the UC-RB NH was likely diminished due to interference caused by the organic moieties present in the UCNP environment. Hence, UC@RB NHs provide higher selectivity in product formation, specifically yielding a greater amount of ascaridole. In addition, the amount required to undergo the photocatalytic reaction was four times higher for UC-RB NHs than for UC@RB NHs, substantially increasing the resources needed. In conclusion, despite the limited recyclability of UC@RB NHs, their use in NIR-triggered photocatalytic reactions proved to be faster, more efficient, and more cost-effective.

When using UC@RB NHs as photocatalysts, RB is not directly excited using the light source; instead, RB is sensitized using the upconverted light from UCNPs, which have a low UCQY. In the photooxidation of α-terpinene, the limiting

Open Access Article. Published on 11 September 2024. Downloaded on 12/28/2024 3:40:09 PM. This article is licensed under a Creative Commons Attribution-NonCommercial 3.0 Unported Licence.

reactant is the singlet oxygen. Therefore, there are numerous steps required to achieve the formation of singlet oxygen: (i) excitation of UCNPs using NIR light; (ii) upconverting the light; (iii) resonant energy transfer from UCNPs to RB; (iii) formation of the RB triplet; (iv) energy transfer from the ^{3}RB to O_2; and (v) formation of $^1O_2$ to finally achieve the photooxidation of α-terpinene. Given these factors, the effectivity of our system is comparable to that described in the most recent literature.[39]

Flow NIR-triggered photooxidations need to be evaluated in the near future for UC@RB NHs. In fact, 85% yield of ascaridole has been reported for RB-sensitized flow photooxidation of α-terpinene.[35,40,41]

Experimental

Synthesis of RB-capped UCNPs

Several UC@RB nanohybrids were synthesized following a previously described procedure.[24] Briefly, six different vials were prepared containing 34.1 mg of UC@BF_4 and increasing concentrations of RB: (1) 4.2×10^{-2}, (2) 4.2×10^{-3}, (3) 4.2×10^{-4}, (4) 4.2×10^{-5}, (5) 4.2×10^{-6}, and (6) 4.2×10^{-7} M in DMF (1 mL total volume). The vials were kept in darkness and stirred at room temperature for 24 h. The corresponding UC@RB nanohybrids were recovered by centrifugation at 12 000*g* for 30 min. Then, the precipitates were washed following cycles of redispersion in 5 mL of DMF and centrifugation at 10 000*g* for 10 min, until the supernatants were transparent. The total volume used for the washing steps was 165 mL for UC@RB1, 270 mL for UC@RB2, 15 mL UC@RB3, and 5 mL for UC@RB4, UC@RB5, and UC@RB6. To eliminate large aggregates, 3 mL of DMF was added and a centrifugation step (1000 g, 2 min) was carried out, thus recovering the supernatant. The final concentrations of the six UC@RB dispersions were calculated by weighing the difference, leaving 100 μL of the dispersion to dry.

Chemical determination of singlet oxygen generation

The singlet oxygen generation upon NIR irradiation of different UC@RB nanohybrids was evaluated in DMF, ACN, and EtOH by using an anthracene derivative as an optical probe (ABDA).[12] An AB2 series spectrofluorometer equipped with a NIR laser diode (980 nm CW, 308 W cm^{-2}) was used for these experiments. In a quartz cuvette, 1 mL of solution containing ABDA (1.03×10^{-5} M) and the corresponding UC@RB nanohybrid (1 mg mL^{-1}) was prepared and kept under stirring and oxygen-saturated conditions. Then, the solution was irradiated with an NIR laser. Subsequently, the ABDA emission spectrum from 398 nm to 550 nm was recorded at different time intervals (λ_{exc} = 378 nm, 750 V, excitation, and an emission bandwidth of 2 nm, 1 nm s^{-1}). The $^1O_2$ generation efficiency was evaluated from the decreases of the ABDA emission at 410 nm.

In addition, a control sample containing UC@RB and ABDA was kept in the dark.

Evaluation of photocatalytic activity of UC@RB nanohybrids

200 μL of a mixture containing the corresponding synthesized UC@RB nanohybrids with different amounts of RB (*i.e.*, UC@RB1, UC@RB2, UC@RB3, UC@RB4, UC@RB5, and UC@RB6) and 0.06 mM of α-terpinene in *N*,*N*′-dimethylformamide-d_7 were placed in a 10 × 10 mm quartz cuvette. To ensure oxygen-saturated solutions, the mixtures were bubbled with oxygen for 15 minutes in an ice bath before irradiation. Then, the cuvette was irradiated with a CW 980 nm laser diode (308 W cm^{-2}) for 8 hours under continuous stirring at 20 °C. After irradiation completion, the reaction mixture was centrifuged at 10 000*g* for 10 min to separate the UC@RB nanohybrids from the reaction. Then, the supernatant was analyzed by ^{1}H-NMR (see more details in ESI, Fig. S19†). Control experiments under identical conditions, but without nanohybrids and using BF_4^--stabilized UCNPs (5 mg mL^{-1}), were also carried out.

Conclusions

UC@RB nanohybrids have been used as near-infrared (NIR) light-harvesting systems for heterogeneous photocatalysis, specifically, for selective photooxidation of α-terpinene with moderate yields (∼50%).

The photophysical events occurring upon NIR-irradiation proved to be strongly dependent on the number of RB molecules anchored to the UCNPs and their aggregation state (the monomer being preferred over the aggregates). The best photocatalytic performance corresponds to a ratio of ∼100 RB/UCNP for UC@RB2 and UC@RB3, which correlates well with their optical properties and the highest ^{3}RB generation. To get the best photocatalytic performance, it is crucial to optimize the synthetic protocol used to prepare UCNHs, the PC concentration, solvent and irradiation time. This study highlights the potential of UC@RB NHs as an efficient and cost-effective NIR photocatalyst and compares it with the covalently linked analogue, UC-RB. The rapid preparation of UC@RB NHs, coupled with their higher selectivity towards the formation of ascaridole and the lower amount of NHs required (5 and 10 mg mL^{-1}), results in a more selective photocatalytic reaction. This efficiency translates into lower material costs, minimized waste, and a smaller environmental footprint, thereby enhancing the sustainability of the process.

Next, the optimization of synthetic protocols for UCNHs comprising non-covalently and covalently linked PCs needs to be accomplished to simultaneously avoid PC leaching and improve recyclability together with flow photooxidation experiments.

Data availability

The data supporting this article have been included as part of the ESI.†

Author contributions

Laura Francés-Soriano: investigation, methodology, data curation, visualization, formal analysis, writing-original draft; Delia Bellezza; investigation, methodology, data curation, visualization, writing – original draft; Juan Ferrera-González: investigation, methodology, data curation, formal analysis; María

© 2024 The Author(s). Published by the Royal Society of Chemistry

Open Access Article. Published on 11 September 2024. Downloaded on 12/28/2024 3:40:09 PM. This article is licensed under a Creative Commons Attribution-NonCommercial 3.0 Unported Licence.

González-Béjar: conceptualization, funding acquisition, project administration, methodology, supervision, writing – original draft; writing – review & editing; Julia Pérez-Prieto: conceptualization, funding acquisition, project administration, supervision, writing – review & editing.

Conflicts of interest

There are no conflicts to declare.

Acknowledgements

This research was funded by Agencia Estatal de Investigación-AEI (grant number MMCIU Unit of Excellence "Maria de Maeztu" CEX2019-000919-M); Ministerio de Universidades (María Zambrano contract L. F. S. (ZA21-037)); and Generalitat Valenciana (IDIFEDER/2018/064 and IDIFEDER/2021/064), all of them partially cofinanced with FEDER funds. This study forms part of the Advanced Materials programme (MFA/2022/051) and was supported by MICIN with funding from European Union NextGenerationEU (PRTR-C17.I1) and by Generalitat Valenciana. We also thank Universitat de Valéncia (Programa Propi del Vicerectorat d'Investigació de la UV (UV-INV_AE-2653809).

References

1 M. González-Béjar, J. Pérez-Prieto and J. C. Scaiano, in *Green Chem.*, Nova Science Publishers, Inc., 2014, pp. 71–105.
2 A. A. Ghogare and A. Greer, *Chem. Rev.*, 2016, **116**, 9994–10034.
3 M. Zamadar and A. Greer, in *Handbook of Synthetic Photochemistry*, 2009, pp. 353–386.
4 M. Freitag, N. Möller, A. Rühling, C. A. Strassert, B. J. Ravoo and F. Glorius, *ChemPhotoChem*, 2019, **3**, 24–27.
5 A. R. Obah Kosso, N. Sellet, A. Baralle, M. Cormier and J. P. Goddard, *Chem. Sci.*, 2021, **12**, 6964–6968.
6 N. Sellet, M. Cormier and J. P. Goddard, *Org. Chem. Front.*, 2021, **8**, 6783–6790.
7 N. Sellet, L. Clement-Comoy, M. Elhabiri, M. Cormier and J. P. Goddard, *Chem.–Eur. J.*, 2023, **29**, 1–8.
8 N. Sellet, M. Sebbat, M. Elhabiri, M. Cormier and J. P. Goddard, *Chem. Commun.*, 2022, **58**, 13759–13762.
9 S. Wu, J. P. Blinco and C. Barner-Kowollik, *Chem.–Eur. J.*, 2017, **23**, 8325–8332.
10 P. Lederhose, Z. Chen, R. Müller, J. P. Blinco, S. Wu and C. Barner-Kowollik, *Angew. Chem., Int. Ed.*, 2016, **55**, 12195–12199.
11 S. Wu and H. J. Butt, *Phys. Chem. Chem. Phys.*, 2017, **19**, 23585–23596.
12 M. González-Béjar, M. Liras, L. Francés-Soriano, V. Voliani, V. Herranz-Pérez, M. Duran-Moreno, J. M. Garcia-Verdugo, E. I. Alarcon, J. C. Scaiano and J. Pérez-Prieto, *J. Mater. Chem. B*, 2014, **2**, 4554–4563.
13 X. Yang, Q. Xiao, C. Niu, N. Jin, J. Ouyang, X. Xiao and D. He, *J. Mater. Chem. B*, 2013, **1**, 2757–2763.
14 F. Chen, S. Zhang, W. Bu, Y. Chen, Q. Xiao, J. Liu, H. Xing, L. Zhou, W. Peng and J. Shi, *Chem.–Eur. J.*, 2012, **18**, 7082–7090.
15 K. Liu, X. Liu, Q. Zeng, Y. Zhang, L. Tu, T. Liu, X. Kong, Y. Wang, F. Cao, S. A. G. Lambrechts, M. C. G. Aalders and H. Zhang, *ACS Nano*, 2012, **6**, 4054–4062.
16 Z. Zhang, J. N. Rahmat, R. Mahendran and Y. Zhang, *Adv. Sci.*, 2020, **7**, 2001831.
17 K. Lv, L. Yao, X. Fu, X. Gao, H. Wang, Y. Zhou, R. Zhang, Y. Lu, J. Feng and H. Zhang, *Nano Today*, 2023, **52**, 101964.
18 S. Cui, H. Chen, H. Zhu, J. Tian, X. Chi, Z. Qian, S. Achilefu and Y. Gu, *J. Mater. Chem.*, 2012, **22**, 4861–4873.
19 S. Cui, D. Yin, Y. Chen, Y. Di, H. Chen, Y. Ma, S. Achilefu and Y. Gu, *ACS Nano*, 2013, **7**, 676–688.
20 Y. Il Park, H. M. Kim, J. H. Kim, K. C. Moon, B. Yoo, K. T. Lee, N. Lee, Y. Choi, W. Park, D. Ling, K. Na, W. K. Moon, S. H. Choi, H. S. Park, S.-Y. Yoon, Y. D. Suh, S. H. Lee and T. Hyeon, *Adv. Mater.*, 2012, **24**, 5755–5761.
21 A. Nsubuga, K. Morice, N. Fayad, F. Pini, V. Josserand, X. Le Guével, A. Alhabi, M. Henry, D. Puchán Sánchez, N. Plassais, P. Josse, J. Boixel, P. Blanchard, C. Cabanetos and N. Hildebrandt, *Adv. Funct. Mater.*, 2024, 2410077.
22 L. Francés-Soriano, M. A. Zakharko, M. González-Béjar, P. A. Panchenko, V. Herranz-Pérez, D. A. Pritmov, M. A. Grin, A. F. Mironov, J. M. García-Verdugo, O. A. Fedorova and J. Pérez-Prieto, *Chem. Mater.*, 2018, **30**, 3677–3682.
23 J. Wu, S. Du and Y. Wang, *J. Mater. Chem. B*, 2019, **7**, 7306–7313.
24 J. Ferrera-González, M. González-Béjar and J. Pérez-Prieto, *Nanoscale*, 2023, **15**, 19792–19800.
25 W. Liu, Y. Zhang, W. You, J. Su, S. Yu, T. Dai, Y. Huang, X. Chen, X. Song and Z. Chen, *Nanoscale*, 2020, **12**, 13948–13957.
26 F. Jin, J. Qi, D. Liu, Y. You, G. Shu, Y. Du, J. Wang, X. Xu, X. Ying, J. Ji and Y. Du, *J. Controlled Release*, 2021, **337**, 90–104.
27 X. Chen, Y. Zhang, X. Zhang, Z. Zhang and Y. Zhang, *Microchim. Acta*, 2021, **188**, 1–10.
28 Y. Wang, K. Liu, X. Liu, K. Dohnalová, T. Gregorkiewicz, X. Kong, M. C. G. Aalders, W. J. Buma and H. Zhang, *J. Phys. Chem. Lett.*, 2011, **2**, 2083–2088.
29 V. Muhr, C. Würth, M. Kraft, M. Buchner, A. J. Baeumner, U. Resch-Genger and T. Hirsch, *Anal. Chem.*, 2017, **89**, 4868–4874.
30 S. Sharma and A. Sharma, *Org. Biomol. Chem.*, 2019, **17**, 4384–4405.
31 F. Ronzani, N. Costarramone, S. Blanc, A. K. Benabbou, M. Le Bechec, T. Pigot, M. Oelgemöller and S. Lacombe, *J. Catal.*, 2013, **303**, 164–174.
32 L. Pessoni, S. Lacombe, L. Billon, R. Brown and M. Save, *Langmuir*, 2013, **29**, 10264–10271.
33 C. Mendoza, N. Emmanuel, C. A. Páez, L. Dreesen, J. C. M. Monbaliu and B. Heinrichs, *ChemPhotoChem*, 2018, **2**, 890–897.
34 G. O. Schenck, *Angew. Chem.*, 1957, **69**, 579–599.
35 Z. Li and Y. Zhang, *Nanotechnology*, 2008, **19**, 345606.

© 2024 The Author(s). Published by the Royal Society of Chemistry

Open Access Article. Published on 11 September 2024. Downloaded on 12/28/2024 3:40:09 PM.
This article is licensed under a Creative Commons Attribution-NonCommercial 3.0 Unported Licence.

36 S. Wilhelm, M. Kaiser, C. Würth, J. Heiland, C. Carrillo-Carrion, V. Muhr, O. S. Wolfbeis, W. J. Parak, U. Resch-Genger and T. Hirsch, *Nanoscale*, 2015, **7**, 1403–1410.
37 M. Bregnhøj, M. Westberg, F. Jensen and P. R. Ogilby, *Phys. Chem. Chem. Phys.*, 2016, **18**, 22946–22961.
38 G. W. Mcgraw, R. W. Hemingway, L. L. Ingram, C. S. Canady and W. B. Mcgraw, *Environ. Sci. Technol.*, 1999, **33**, 4029–4033.
39 J. Chen, R. Prinsloo and X. Ni, *Technologies*, 2024, **12**, 29.
40 N. P. Beard and A. J. De Mello, *Electrophoresis*, 2002, **23**, 1722–1730.
41 M. C. Mitchell, V. Spikmans and A. J. De Mello, *Analyst*, 2001, **126**, 24–27.

© 2024 The Author(s). Published by the Royal Society of Chemistry